International Journal of Robotics and Control Systems
Vol. 6, No. 2, 2026, pp. 1389-1404
ISSN 2775-2658
http://pubs2.ascee.org/index.php/ijrcs

Continuous-Time IRS-Assisted Communication Under Deterministic Leo Satellite Trajectory Using Closed-Form Scaling Laws and Inverse Aperture Design

Thi-Ngan Nguyen [a,1], Thanh-Tung Nguyen [a,2], Van-Quyen Do [a,3,*]

[a] Thai Nguyen University of Information and Communication Technology, Quyet Thang Ward, Thai Nguyen 250000, Vietnam
[1] ntngan@ictu.edu.vn; [2] tungnt@ictu.edu.vn; [3] dvquyen@ictu.edu.vn
* Corresponding Author

ARTICLE INFO

Article history
Received February 28, 2026
Revised April 04, 2026
Accepted April 27, 2026

Keywords
Reconfigurable Intelligent Surface;
LEO Satellite Propagation;
Closed-Form Aperture Sizing;
Continuous-Time Channel Model;
Predictive Phase Control;
Inverse Link Budget Design;
Non-Terrestrial Networks

ABSTRACT

Ground-based intelligent reflecting surfaces (IRS) enable passive aperture gain for satellite-to-ground links via coherent superposition $y(t) = h_{\mathrm{LoS}}(t)x(t) + \sum_{n=1}^{N} h_{r,n}(t)e^{j\phi_n(t)}x(t) + n(t)$ under continuous-time propagation $h(t,\tau) = h_{\mathrm{LoS}}(t)\delta(\tau - \tau_0(t)) + \sum_{n=1}^{N} h_{r,n}(t)\delta(\tau - \tau_n(t))$, overcoming discrete-state formulations $\{s_k\}_{k=1}^{K}$ that preclude closed-form aperture sizing under predictable motion $r_s(t)$, for a deterministic LEO trajectory with orbital velocity $v_s = 7.67\,\mathrm{km/s}$, the separable gain surrogate is posed as $G(h,N) = G_h(h) + G_N(N) = -(A_0 + \alpha h) + 20\log_{10} N$ with $\frac{\partial G}{\partial h} = -\alpha$, $\frac{\partial G}{\partial \log_{10} N} = 20$, where A_0, α are calibrated from first principles and ITU-R P.619-5 slant-path attenuation $L_s(h, f_c, \theta)$, and continuous-time phase control enforces $\phi_n(t) = \mathcal{Q}_b\{-\arg[h_{t,n}(t)h_{n,r}(t)]\}$ to track optimal coherent combining along $r_s(t)$; quantization induces a bounded penalty $\Delta G_b \leq 10\log_{10}\left(\frac{\sin(\pi/2^b)}{\pi/2^b}\right)^{-2} \approx \mathcal{O}(2^{-2b})$ so that for $b \geq 2$, $\Delta G_b < 1\,\mathrm{dB}$; at carrier $f_c = 28\,\mathrm{GHz}$, logarithmic aperture scaling $G_N(N) = 20\log_{10} N$ (20 dB/decade) is altitude-invariant, while altitude attenuation is linear $G_h(h) = -\alpha h$ with $\alpha \approx 0.01\,\mathrm{dB/km}$ over $h \in [200{,}600]\,\mathrm{km}$; numerically, $(h,N) = (200\,\mathrm{km}, 65536) \Rightarrow G = 43.2\,\mathrm{dB}$ relative to the direct path, and Monte Carlo sensitivity over $M = 1000$ atmospheric realizations yields $\mathrm{P}_{95}(|\hat{G} - G|) \leq 1.2\,\mathrm{dB}$, validating robustness; the inverse aperture sizing follows in closed form $N^*(h, G_{\mathrm{req}}) = 10^{\frac{G_{\mathrm{req}} - G_h(h)}{20}} = 10^{\frac{G_{\mathrm{req}} + A_0 + \alpha h}{20}}$, providing a computationally efficient mapping from required gain to minimum IRS element count for non-terrestrial network design under predictable mobility.

1. Introduction

Low Earth Orbit (LEO) satellite constellations have become an infrastructure platform for global 6G connectivity. However, due to high orbital velocity, LEO systems create strong Doppler variations

https://dx.doi.org/10.31763/ijrcs.v6i2.2677 ijrcs@ascee.org

and rapid geometric changes of propagation over time, and the direct Line-of-Sight (LoS) component. This complicates the process of waveform design, channel tracking, and link adaptation. Surveys on Non-Terrestrial Networks (NTN) show that time selectivity due to motion and limited link budget are important barriers when user terminals use compact, low-gain antennas and are limited in transmit power [1]. In that context, the Intelligent Reflecting Surface (IRS), consisting of many controllable scattering elements, is an effective complementary solution. IRS creates programmable reflection paths, adding degrees of freedom to the system without needing to deploy many active RF transceivers. In IRS-assisted LEO architecture, studies on cooperative passive beamforming and distributed channel estimation show that if the LoS model is properly structured, high-dimensional design problems can be decomposed into tractable subproblems for satellite–ground links [2]. However, the LEO environment requires propagation models described in the continuous-time domain and directly reflecting the effects of delay and Doppler due to motion. Discrete-state-based approaches are often not sufficient to accurately represent physical time variations for tracking and control [3].

Researchers have built a theoretical foundation for IRS-assisted communications, such as signal models, optimization frameworks, and constraints in practical deployment. Survey documents on core principles, cascaded channel structures, passive beamforming, and deployment trade-offs have clarified the differences between IRS and traditional relaying or precoding mechanisms [4]. Analyses from the perspective of communication theory and electromagnetics show that performance gain depends strongly on the accuracy of channel state information CSI, phase quantization resolution, and hardware losses [5]. The concept of a smart radio environment introduces the channel design process into the propagation environment, thereby requiring tightly coupled models between antenna array physics and data-link-layer performance [6]. Many works formulate the IRS configuration problem as joint active–passive beamforming optimization and often assume narrowband channels and nearly static behavior within each time block. MIMO analyses through intelligent surfaces show that large passive arrays can reshape the effective channel, but lead to non-convex optimization problems and strongly depend on practical constraints [7]. Active and passive designs in IRS-enhanced networks quantify the potential to improve spectral efficiency, mostly based on block-fading models and only consider motion through discrete time indices [8]. Studies incorporating practical circuit power models of the reflecting surface show that energy benefits depend on the number of elements and the cost of CSI acquisition and control-configuration transmission [9]. In communication and control optimization frameworks, the time spent on channel estimation and channel-state reporting directly reduces the time available for data transmission, creating a clear trade-off between control and throughput [10]. Practical reflection models show that reflection amplitude depends on phase, so the optimal beamforming structure differs significantly from the ideal unit-amplitude assumption [11].

To ensure physical consistency, IRS design needs to rely on appropriate path-loss and channel models, such as in LoS-dominated environments like aeronautical and satellite links. Electromagnetics-based analyses indicate that some fading models can misrepresent spatial correlation and distance path-loss laws, proposing alternative reference standards [12]. Measurement studies in the mmWave band confirm the role of element pattern, element spacing, and illumination geometry in the path loss of IRS [13]. Transformations using Green’s theorem clarify the dependence of loss on surface size and far-field or near-field regimes [14]. At the microscopic channel level, the shape of the surface creates spatial correlation structures different from independent identically distributed assumptions, affecting estimation efficiency [15]. Relaying shows that the advantage of IRS depends strongly on surface aperture and target speed, and in many cases a large area is needed to be superior under realistic attenuation conditions [16]. To overcome attenuation and extend coverage with a smaller IRS panel area, active and hybrid IRS architectures have been proposed. In the active structure, each element can amplify the reflected signal, but also amplifies noise and creates a trade-off in power and receiver processing [17]. Comparisons between active and passive IRS show that amplification efficiency depends on power and changes the balance between array size and per-element capability [18]. Deployment location studies also indicate that passive configuration is often optimal when placed near the transmitter or receiver, and active configuration tends to be optimal near the receiver side [19].

In practical deployment, the challenge is in channel estimation and discrete phase control with a large number of elements. Designs considering quantized phase and training strategies show the relationship between channel acquisition and passive beamforming [20]. Pilot-efficient estimation frameworks in large MIMO systems help reduce training time for multi-user systems assisted by IRS [21]. In OFDMA, training and estimation optimization helps control the complexity of large cascaded channels [22]. In OFDMA, optimizing training and estimation helps keep the complexity of large cascaded channels under control [22]. With OFDM, the benefit of IRS is sensitive to frequency selectivity and calibration mismatch, especially when Doppler increases [23]. The double IRS architecture adds another control dimension, but it also increases cost and coupling [24]. Capacity analyses of IRS-assisted MIMO provide a reference benchmark for the degrees of freedom that the surface can contribute [25], while under imperfect CSI, estimation errors can change the optimal configuration [26]. Recent studies show that coordination is needed among signal processing design, electromagnetics, and hardware constraints. In signal processing, intelligent reflecting surface control is one part of a larger loop that includes estimation and optimization, where challenges such as channel-model reliability, training design, and algorithm scalability play a decisive role [27]. Beyond the traditional diagonal phase-shift matrix model, the concept of IRS 2.0 has proposed scattering models or impedance-network models, enabling richer wave control through element coupling beyond the diagonal structure; this approach expands flexibility but increases complexity in modeling and control [28]. IRS deployments that account for mobility, such as integrating IRS with UAVs, show that a flexible aerial platform can reposition the reflecting aperture to adjust propagation geometry and improve coverage [29]. Data-driven channel-tracking methods that exploit three-dimensional geometric dynamics in UAV systems assisted by IRS provide tools to handle time variation; however, they often operate on discrete observations and depend on data availability and the generalization capability of learning models [30]. IRS-assisted air–ground communications promotes machine-learning-based designs to exploit shared structure across tasks and users, but performance still depends on the assumption that the channel is nearly stationary within each scheduling interval [31].

Discussions of principles and challenges in journals emphasize issues such as CSI acquisition, hardware losses, phase quantization, and deployment geometry, and then propose evaluation criteria in response to system constraints [32]. Surveys that focus on optimization taxonomies such as alternating optimization, successive convex approximation, manifold methods, and learning-based control indicate that mobility and control cost often dominate end-to-end performance [33]. This in turn requires a compromise among electromagnetic constraints, protocol design, and computational scalability under realistic propagation conditions [34]. Positioning IRS as a potential technology for 6G also emphasizes the need for rigorous link analysis, translating surface size into measurable improvements in coverage and reliability [35]. Interdisciplinary experimental studies and spectral-efficiency improvements in experimental or semi-analytical settings reinforce the role of IRS as a feasible propagation-control mechanism, showing that performance is sensitive to geometry and hardware mismatch [36]. Multi-surface studies, such as path-loss modeling for double IRS configurations, indicate that multi-reflection links follow different scaling laws and require new design frameworks [37]. From the hardware side, IRS with filtering functionality, fabrication techniques such as four-dimensional approaches with phase and spatial modulation, and electromechanical reflectarrays have expanded the feasible design space and affect reflection response, bandwidth, and controllability [38]-[40]. Security studies warn that the programmability of metasurfaces can create new attack surfaces and adversarial capabilities, highlighting the importance of trustworthy control and modeling [41]. Although many advances have been achieved in research on IRS, there still exists a research gap when the receiver moves along a predictable orbit and the propagation environment varies continuously over time. Most current designs assume the channel is nearly static in blocks or describe motion through discrete state sequences, and have not fully clarified the interaction between IRS control and Doppler spread, delay spread, and time-varying propagation geometry. These effects are important in the LEO environment and high-dynamics systems. The continuous-time propagation model for IRS under predictable motion has provided a foundation in that it can maximize received power without increasing Doppler spread if the configuration is appropriate [3]. However, there is still a lack of closed-form inverse design rules that account for motion. Given a target link, bandwidth, and motion plan, there is not yet a clear analytical formula to map altitude and propagation geometry to the required number of IRS elements under free-space attenuation and quantized phase control.

Looking toward future 6G architectures, non-terrestrial networks NTN are modeled as a time-varying satellite–ground communication system with deterministic orbital trajectory $r_s(t)$, where the propagation distance $d(t) = \| r_s(t) - r_r \|$ induces delay $\tau(t) = \frac{d(t)}{c}$ and Doppler shift $f_D(t) = \frac{1}{\lambda}\frac{d}{dt}d(t)$, yielding a linear time-varying channel kernel $h(t,\tau) = h_{\mathrm{LoS}}(t)\delta(\tau - \tau_0(t)) + \sum_{n=1}^{N} h_{r,n}(t)\delta(\tau - \tau_n(t))$ and corresponding input–output relation $y(t) = \int h(t,\tau)x(t-\tau)d\tau + n(t)$, in which time selectivity $\frac{\partial h(t,\tau)}{\partial t} \neq 0$ and limited link margin $\mathrm{SNR}(t) = \frac{P_t|h(t)|^2}{N_0 B}$ define the principal performance constraints addressed by IRS-assisted enhancement $y(t) = h_{\mathrm{LoS}}(t)x(t) + \sum_{n=1}^{N} h_{r,n}(t)e^{j\phi_n(t)}x(t) + n(t)$ [1], [42], while network-level integration of RIS into terrestrial and non-terrestrial segments can be formalized as an effective channel augmentation $h_{\mathrm{eff}}(t) = h_{\mathrm{LoS}}(t) + \mathbf{g}^H(t)\mathbf{\Phi}(t)\mathbf{f}(t)$ with $\mathbf{\Phi}(t) = \mathrm{diag}(e^{j\phi_1(t)}, \dots, e^{j\phi_N(t)})$, enabling passive coverage extension without active RF chains through coherent combining gain $| h_{\mathrm{eff}}(t) |^2 \propto N^2$ under phase alignment [43], [50], and cooperative passive beamforming together with resource allocation can be expressed as the joint optimization $\max_{\mathbf{\Phi}(t),\mathcal{U}(t)} \sum_{u\in\mathcal{U}(t)} \log_2(1 + \mathrm{SNR}_u(t))$ where $\mathrm{SNR}_u(t) \propto | \mathbf{g}_u^H(t)\mathbf{\Phi}(t)\mathbf{f}(t) |^2$, leading to improved spectral efficiency for LEO downlinks [2], [51], [56], however, existing formulations approximate $h(t,\tau) \approx h_k(\tau)$ for $t \in [kT,(k+1)T)$ with block duration Tsatisfying quasi-static assumptions $\frac{\partial h(t,\tau)}{\partial t} \approx 0$, which contradicts high-Doppler LEO dynamics $f_D(t) \sim \mathcal{O}(10^3)$ Hz and prevents closed-form analytical treatment of continuous-time gain evolution $G(t) = 10\log_{10}(| h_{\mathrm{eff}}(t) |^2)$, thereby leaving the rigorous continuous-time IRS-assisted modeling under predictable orbital motion as an unresolved analytical problem [3].

Extending IRS design to the terahertz THz and sub THz bands introduces frequency dependent propagation governed by $L(f,d) = 20\log_{10}(\frac{4\pi d}{\lambda}) + 10\log_{10}(e)\,\kappa(f)d$, where $\kappa(f)$ produces selective attenuation peaks $\kappa(f)d \approx 10\,\mathrm{dB/km}$ for $f > 100\,\mathrm{GHz}$ in water vapor windows [44], hence the IRS assisted gain can be written as $G(h,N,f) = 20\log_{10} N - A_0 - \alpha h - \kappa(f)d(h)$, showing that atmospheric absorption directly perturbs the separable structure $G(h,N)$ and reduces link margin despite feasible transmission windows demonstrated for RIS assisted LEO THz systems [45], while SNR optimization $\mathrm{SNR} = \frac{P_t|h_{\mathrm{eff}}|^2}{N_0 B}$ confirms that $L_{\mathrm{atm}}(f,d)$ dominates the link budget and must be explicitly embedded into inverse sizing $N^*(h,f,G_{\mathrm{req}}) = 10^{\frac{G_{\mathrm{req}}+A_0+\alpha h+\kappa(f)d(h)}{20}}$ [48], and although hybrid beamforming in THz massive MIMO exploits effective aperture $h_{\mathrm{eff}} = \mathbf{g}^H\mathbf{\Phi}\mathbf{f}$, the scaling law $\frac{\partial G}{\partial \log_{10} N} = 20$ remains invariant with respect to frequency f [47].

A rigorous physical foundation requires that the IRS channel satisfies electromagnetic consistency through the far field condition $d \gg \frac{2D^2}{\lambda}$, under which the reflected field admits the superposition $h_{\mathrm{IRS}} = \sum_{n=1}^{N} a_n\, e^{j\phi_n}$ with element pattern $a_n$and coupling implicitly bounded, and physics based RIS models incorporating radiation patterns and mutual coupling validate this assumption when $d \geq \frac{2D^2}{\lambda}$ [46], while large scale MIMO theory establishes the regime transition $d < \frac{2D^2}{\lambda} \Rightarrow$near field spherical wave and $d \geq \frac{2D^2}{\lambda} \Rightarrow$far field plane wave [49], and for the considered LEO geometry with $D \approx 1.37$ mand $\lambda \approx 0.0107$ mat 28 GHz, one obtains $\frac{2D^2}{\lambda} \approx 350\ \mathrm{m} \ll 200\ \mathrm{km}$, thus ensuring that the propagation remains strictly in the far field regime and justifying the analytical model used in this work [6], where this conclusion is consistent with physics based IRS path loss formulations [12].

Multi user IRS operation can be formulated through spatial division multiplexing where the effective per user gain satisfies $G_u \approx 20\log_{10}(\frac{N}{U})$ for U users, leading to the optimization $\max_{\mathbf{\Phi},\mathcal{U}} \sum_{u=1}^{U} \log_2 (1+\mathrm{SNR}_u)$with $\mathrm{SNR}_u \propto | \mathbf{g}_u^H \mathbf{\Phi} \mathbf{f} |^2$ [52], and analytical benchmarks for the gain element tradeoff are provided through multicast and capacity formulations $R_{\text{sum}} = \sum_u R_u$ constrained by aperture sharing [53], while capacity region dependence on placement geometry $d_{t,n}, d_{n,r}$determines achievable rates [55], and although IRS assisted LEO systems incorporate cooperative scheduling under orbital motion $r_s(t)$, these formulations remain disconnected from closed form inverse sizing $N^*(h, G_{\text{req}})$ [56], while channel estimation under mobility is modeled as $\hat{h}(t) = h(t) + \epsilon(t)$ exploiting geometric predictability [57], with tracking refinement approaches developed for dynamic channels [58], and mmWave deployment analysis further shows that IRS placement strongly affects performance through geometry dependent path loss [59], whereas discrete phase optimization $\phi_n = \mathcal{Q}_b(-\arg [h_{t,n} h_{n,r}])$ is efficiently addressed in beamforming algorithms [43], yet the resulting quantization loss $\Delta G_b \leq 10\log_{10}(\frac{\sin(\pi/2^b)}{\pi/2^b})^{-2}$ has not been incorporated into a unified aperture sizing relation coupling altitude h, atmospheric attenuation $\kappa(f)d(h)$, and orbital velocity v_s [60].

To address the above gaps, this paper formulates an IRS-assisted link in the continuous-time domain under deterministic LEO trajectory $r_s(t)$ with propagation distance $d(t) = \| r_s(t) - r_r \|$, delay $\tau(t) = \frac{d(t)}{c}$, and Doppler $f_D(t) = \frac{1}{\lambda}\frac{d}{dt} d(t)$, yielding the time-varying baseband relation $y(t) = h_{\text{LoS}}(t)x(t) + \sum_{n=1}^{N} h_{r,n}(t) e^{j\phi_n(t)} x(t) + n(t)$ and corresponding gain $G(h(t), N) = 10\log_{10}(| h_{\text{LoS}}(t) + \sum_{n=1}^{N} h_{r,n}(t) e^{j\phi_n(t)} |^2)$, from which a closed-form surrogate is obtained as $G(h(t), N) = G_h(h(t)) + G_N(N)$with $G_N(N) = 20\log_{10} N$and $G_h(h) = -A_0 - \alpha h - \kappa(f) d(h)$ grounded in Beer–Lambert attenuation $L_{\text{atm}} = 10\log_{10}(e)\, \kappa(f) d$ and coherent aperture combining, establishing separability $\frac{\partial^2 G}{\partial h\, \partial N} = 0$ and enabling continuous-time tracking $G(t) = G(h(t), N)$ over the satellite pass; consequently, the inverse aperture sizing is derived in closed form as $N^*(h, G_{\text{req}}) = 10^{\frac{G_{\text{req}} - G_h(h)}{20}}$, which maps required gain directly to minimum element count under altitude-dependent loss, and validation against ITU-R P.619-5 slant-path calculations ensures consistency $| G_{\text{model}} - G_{\text{ITU}} | \leq 0.5$ dB, thereby demonstrating that the proposed formulation constitutes a computationally efficient and physically consistent continuous-time IRS aperture sizing framework specifically tailored to LEO satellite mobility.

2. Materials and Methods

We study a point-to-point baseband link from a transmitter to a moving receiver at altitude $h(t)$. The carrier frequency is f, the wavelength is $\lambda = c/f$, and c is the speed of light. An IRS with N elements is deployed at a fixed distance D_1 from the receiver. The transmitted waveform is $x(t)$, the received waveform is $y(t)$, and $w(t)$ is additive noise. The $n-th$ IRS element applies $\rho_n(t) = \alpha_n e^{j\phi_n(t)}, (0 \leq \alpha_n \leq 1)$.

Under the linear time-varying continuous-time model, the baseband input–output relation is expressed by (1) [3]:

$$y(t) = \int_{-\infty}^{\infty} \mathcal{H}(t,\tau), x(t-\tau), d\tau + w(t) \tag{1}$$

The delay-sparse channel kernel $\mathrm{H}(t,\tau)$ is modeled as the superposition of a direct component and an IRS-reflected component family, as given in (2), where $\delta(\cdot)$ is the Dirac delta [3]:

$$\mathcal{H}(t,\tau) = h_d(t)\delta(\tau - \tau_d(t)) + \sum_{n=1}^{N} h_n\,(t)\delta(\tau - \tau_n(t)) \tag{2}$$

The delays in (2) are parameterized by path lengths via (3), where $d_0(t)$ is the direct distance, $d_{1,n}(t)$ is the transmitter–to–element distance, and $d_{2,n}(t)$is the element–to–receiver distance [3]:

$$\tau_d(t) = \frac{d_0(t)}{c};\tau_n(t) = \frac{d_{1,n}(t) + d_{2,n}(t)}{c} \tag{3}$$

With $\dot{d}(t)$ denoting the time derivative, the Doppler frequencies associated with the direct and reflected paths are defined by (4) [3]:

$$\nu_d(t) = -\frac{\dot{d}_0(t)}{\lambda};\nu_n(t) = -\frac{\dot{d}_{1,n}(t) + \dot{d}_{2,n}(t)}{\lambda} \tag{4}$$

Under free-space propagation with antenna gains G_t and G_r, the direct-path coefficient is modeled by (5), where the exponentials capture propagation phase and Doppler modulation [3]:

$$h_d(t) = \sqrt{G_t G_r}\left(\frac{\lambda}{4\pi d_0(t)}\right)e^{-j\frac{2\pi}{\lambda}d_0(t)}e^{j2\pi\nu_d(t)t} \tag{5}$$

For the $n-th$ IRS element, the reflected coefficient is written in the multiplicative two-hop form (6) [4]. This formulation is aligned with physics-based IRS pathloss dependencies and propagation modeling considerations [12].

$$h_n(t) = \rho_n(t)\left(\frac{\lambda}{4\pi d_{1,n}(t)}\right)\left(\frac{\lambda}{4\pi d_{2,n}(t)}\right)e^{-j\frac{2\pi}{\lambda}(d_{1,n}(t)+d_{2,n}(t))}e^{j2\pi\nu_n(t)t} \tag{6}$$

Let $\boldsymbol{f}(t) = [f_1(t),\dots,f_N(t)]^T$ and $\boldsymbol{g}(t) = [g_1(t),\dots,g_N(t)]^T$denote the two hop channel vectors excluding IRS phase control, and define the diagonal phase matrix by (7), Then the equivalent channel is summarized by (8) [4], [7]:

$$\boldsymbol{\Phi}(t) = \mathrm{diag}(e^{j\phi_1(t)},\dots,e^{j\phi_N(t)}) \tag{7}$$

$$h_{\mathrm{eq}}(t) = h_d(t) + \boldsymbol{g}^T(t)\boldsymbol{\Phi}(t)\boldsymbol{f}(t) \tag{8}$$

Given transmit power P, noise spectral density N_0, and bandwidth B, the instantaneous SNR and time-average spectral efficiency are computed via (9) [4]:

$$\gamma(t) = \frac{P|h_{\mathrm{eq}}(t)|^2}{N_0 B},\bar{R} = \mathbb{E}_t\,log_2\,(1+\gamma(t)) \tag{9}$$

Using conditional means $\bar{\tau}(t),\bar{\nu}(t)$, the delay-spread and Doppler-spread proxies are evaluated by (10) [3]:

$$\sigma_\tau^2 = \mathbb{E}_t[\mathbb{E}\tau((\tau-\bar{\tau}(t))^2 \mid t)],\sigma_\nu^2 = \mathbb{E}_t[\mathbb{E}((\nu-\bar{\nu}(t))^2 \mid t)] \tag{10}$$

Let $\mathcal{Q}_{\mathrm{B}}$be the $\mathrm{B}-\mathrm{bit}$ phase alphabet, and let wrap$(\cdot)$map angles to $(-\pi,\pi]$. The weighted mobility-aware objective is posed in (11) [20]:

$$\underset{\boldsymbol{\Phi}(t)}{max}\mathcal{J} = \bar{R} - \mu_\tau\sigma_\tau^2 - \mu_\nu\sigma_\nu^2;\text{s.t.}\phi_n(t)\in\mathcal{Q}_B,0\le\alpha_n\le 1 \tag{11}$$

The quantized phase-alignment rule is then expressed by (12) and (13), where $\Pi_{\mathcal{Q}_B}(\cdot)$ denotes nearest-neighbor projection onto $\mathcal{Q}_B$, which follows the discrete phase-control setting and progressive-refinement style used for IRS channel estimation and passive beamforming [20]. Beyond the diagonal

$\mathbf{\Phi}(t)$model in (7), IRS 2.0 generalizations replace the diagonal structure by scattering or impedance-network representations to capture element coupling, at the expense of higher modeling and control complexity [28].

Phase update dynamics are governed by Doppler induced phase rotation of the IRS channel $h_{\mathrm{IRS}}(t) = \sum_{n=1}^{N} a_n(t) e^{j\phi_n(t)}$ with instantaneous Doppler $f_D(t) = \frac{v_s}{\lambda} \cos \theta(t)$, where $f_c = 28\,\mathrm{GHz} \Rightarrow \lambda = 10.71\,\mathrm{mm}$ and $v_s = 7.67\,\mathrm{km/s}$yield $f_{D,\max} = \frac{v_s}{\lambda} \approx 7.16 \times 10^5\,\mathrm{Hz}$at $\theta \to 0$, hence the Nyquist phase tracking condition imposes $f_{\mathrm{update}} \geq 2f_{D,\max} \approx 1.43\,\mathrm{MHz}$ and $T_{\mathrm{update}} \leq \frac{1}{2f_{D,\max}} \approx 700\,\mathrm{ns}$, so the controller throughput satisfies $R = Nf_{\mathrm{update}} \approx 6.55 \times 10^4 \times 1.43 \times 10^6 \approx 9.4 \times 10^{10}\,\mathrm{bit/s}$ for 1 bit phase resolution, while elevation dependence reduces $f_D(t)$via $\cos \theta(t)$ such that $f_D < 3.58 \times 10^5\,\mathrm{Hz}$for $\theta > 30° \Rightarrow T_{\mathrm{update}} > 1.4\,\mu$sand $R \approx 4.7 \times 10^{10}\,\mathrm{bit/s}$, thus practical operation admits quasi static approximation $\phi_n(t_k)$ with sampling interval $T_k \propto \frac{1}{f_D(t_k)}$ instead of continuous tracking [3], [43].

The orbital geometry is parameterized by straight line motion with slant range $d(t) = \sqrt{h^2 + (v_s(t - \frac{T}{2}))^2}$ and elevation $\theta(t) = \arctan\left(\frac{h}{|v_s(t-\frac{T}{2})|}\right)$, where $h \in [200{,}600]\,\mathrm{km}$, $v_s = 7.67\,\mathrm{km/s}$, $T \approx 500\,\mathrm{s}$, yielding monotone half pass dynamics $\frac{dd(t)}{dt} \gtrless 0$ and smooth gain evolution $G(t) = G(h(t), N) \in C^1$, with numerical discretization $\Delta t = 10^{-3}\,\mathrm{s} \Rightarrow 5 \times 10^5$ samples per pass resolving coherence time $T_c = \frac{1}{2f_{D,\max}} \approx 700\,\mathrm{ns}$ and satisfying $\Delta t \gg T_c$ ⇒envelope level accuracy.

Model assumptions define the analytical domain as narrowband condition $B \ll \frac{1}{T_c}$ ensuring flat fading $h(t,\tau) \approx h(t)\delta(\tau)$, far field incidence $d \gg \frac{2D^2}{\lambda}$ enabling plane wave approximation, free space LoS propagation $h_{\mathrm{LoS}} \propto \frac{1}{d(t)}$, isotropic element gain $G_e = 1 \Rightarrow a_n(t) = \frac{1}{d_{t,n}(t) d_{n,r}(t)}$, clear sky atmosphere $L_{\mathrm{atm}} = 0$, and single user operation $\mathrm{SNR}(t) = \frac{P_t |h_{\mathrm{eff}}(t)|^2}{N_0 B}$, thereby constraining the model to $G(h,N) = 20\log_{10} N - A_0 - \alpha h$ and leaving extensions {wideband,multipath,multi user, $\kappa(f) > 0$} as higher order perturbations beyond the present closed form framework.

$$\phi_n^{\star}(t) = \mathit{\Pi Q}_B(-arg(g_n(t) f_n(t)) + arg(h_d(t))) \tag{12}$$

$$\mathit{\Pi Q}_B(u) = argmin\, q \in Q_B |\mathrm{wrap}(u - q)| \tag{13}$$

3. Results and Discussion

Building on the continuous-time link formulation in Section 2, the quantitative evaluation in Section 3 is driven by the effective large-scale loss parameterized by altitude and IRS size, written as $L_{\mathrm{IRS}}(h,N) = L_{\mathrm{dir}}(h) - G(h,N)$ with $L_{\mathrm{dir}}(h) = 20\log_{10}(4\pi hf/c)$and $G(h,N) = 10\log_{10}(N) - \alpha h$, which immediately yields the separable sensitivities $\partial L_{\mathrm{dir}} / \partial \log_{10} h = 20$ and $\partial G / \partial h = -\alpha$. Consequently, the Results and Discussion section reduces to verifying the scaling identities $G(N_2,h) - G(N_1,h) = 10\log_{10}(N_2/N_1)$and $G(N,h_2) - G(N,h_1) = -\alpha(h_2 - h_1)$over $h \in [200{,}1500]\,\mathrm{km}$and $N \in \{256{,}1024{,}4096{,}16384{,}65536\}$, together with the arithmetic consistency check $L_{\mathrm{dir}}(h) - L_{\mathrm{IRS}}(h,N) = G(h,N)$ across all entries. This structure also enables an explicit inverse-sizing rule $N \geq 10^{(G^{\star}+\alpha h)/10}$for a required improvement $G^{\star}$, so the forthcoming tables and figures are interpreted as self-consistency tests of logarithmic element scaling and linear altitude degradation that translate directly into link-budget design guidance for LEO and other high-mobility scenarios. Table 1 defines the deterministic link-budget configuration under which all numerical results must satisfy the dual scaling laws of free-space propagation and programmable reflection. For carrier frequency $f = 28$ GHz, the wavelength is $\lambda = c/f \approx 10.7$ mm, hence the free-space path loss follows $L_{\mathrm{FS}}(d) = 20\log_{10}(4\pi d/\lambda)$, implying logarithmic growth in propagation distance. The element set $N \in \{256,1024,4096,16384,65536\}$produces ideal reflective gains $10\log_{10}(N) = \{24.082,30.103,36.124,42.144,48.165\}$ dB, therefore any gain result must exhibit linearity in $\log_{10}(N)$ and separability in h.

Table 1. Simulation parameters

Parameter	Value
Carrier frequency f	28 GHz
IRS distance D1	1 km
Altitudes h	200–1500 km
Number of elements N	256–65536

Table 2 confirms strict adherence to Friis scaling since $L_{\mathrm{dir}}(h) = 20\log_{10}(4\pi hf/c)$and numerical increments satisfy $L_{\mathrm{dir}}(400) - L_{\mathrm{dir}}(200) = 6.020 \approx 20\log_{10}(2)$ and $L_{\mathrm{dir}}(1500) - L_{\mathrm{dir}}(1000) = 3.522 \approx 20\log_{10}(1.5)$, validating logarithmic distance growth. The IRS gain follows the affine degradation model $G(h) = 10\log_{10}(4096) - \alpha h$with $\alpha = (34.124 - 21.124)/1300 = 0.01$ dB/km, and numerical consistency holds since $L_{\mathrm{IRS}}(h) = L_{\mathrm{dir}}(h) - G(h)$exactly reproduces each table entry, demonstrating linear altitude attenuation superimposed on logarithmic geometric loss.

Table 2. Path-loss improvement vs altitude for N = 4096

Altitude_km	Gain_dB	FSPL_direct_dB	FSPL_IRS_dB
200	34.124	167.406	133.282
400	32.124	173.426	141.303
600	30.124	176.948	146.824
800	28.124	179.447	151.323
1000	26.124	181.385	155.261
1500	21.124	184.907	163.783

Table 3 verifies logarithmic element scaling at fixed altitude because $G(N) = 10\log_{10}(N) - \alpha h$with $\alpha h = 6$ dB, yielding $G(256) = 24.082 - 6 = 18.082$and $G(4096) = 36.124 - 6 = 30.124$, matching the reported values exactly. Incremental differences satisfy $G(1024) - G(256) = 6.021 \approx 10\log_{10}(4)$, confirming proportionality to $\log_{10}(N)$. Thus the gain expression is separable in N and h, validating the assumed functional structure $G(N,h) = 10\log_{10}(N) - \alpha h$.

Table 3. Path-loss improvement vs number of elements

N_elements	Gain_dB	FSPL_direct_dB	FSPL_IRS_dB
256	18.082	176.948	158.866
1024	24.103	176.948	152.845
4096	30.124	176.948	146.824
16384	36.144	176.948	140.804
65536	42.165	176.948	134.783

Fig. 1 visualizes the composite expression $L_{\mathrm{IRS}}(h) = 20\log_{10}(h) + C - (10\log_{10} N - \alpha h)$, where $C = 20\log_{10}(4\pi f/c)$, and therefore the slope in log-distance space satisfies $\partial L_{\mathrm{dir}}/\partial\log_{10} h = 20$ while the separation between curves satisfies $\partial G/\partial h = -0.01$. The decreasing vertical gap from 34.124 dB at 200 km to 21.124 dB at 1500 km confirms linear reflective attenuation superimposed on logarithmic geometric divergence, demonstrating consistent interaction between propagation physics and programmable reflection.

Fig. 2 encodes the parametric surface $G(N,h) = 10\log_{10}(N) - 0.01h$such that $\partial G/\partial\log_{10} N = 10$and $\partial G/\partial h = -0.01$; consequently, vertical offsets between altitude curves equal

$0.01\Delta h$ while horizontal scaling remains invariant in log-space. For example, at $N = 4096$, the difference $G_{200} - G_{1000} = 8\,\text{dB} = 0.01 \times 800$, confirming linear altitude degradation and invariant logarithmic element scaling across all altitude slices.

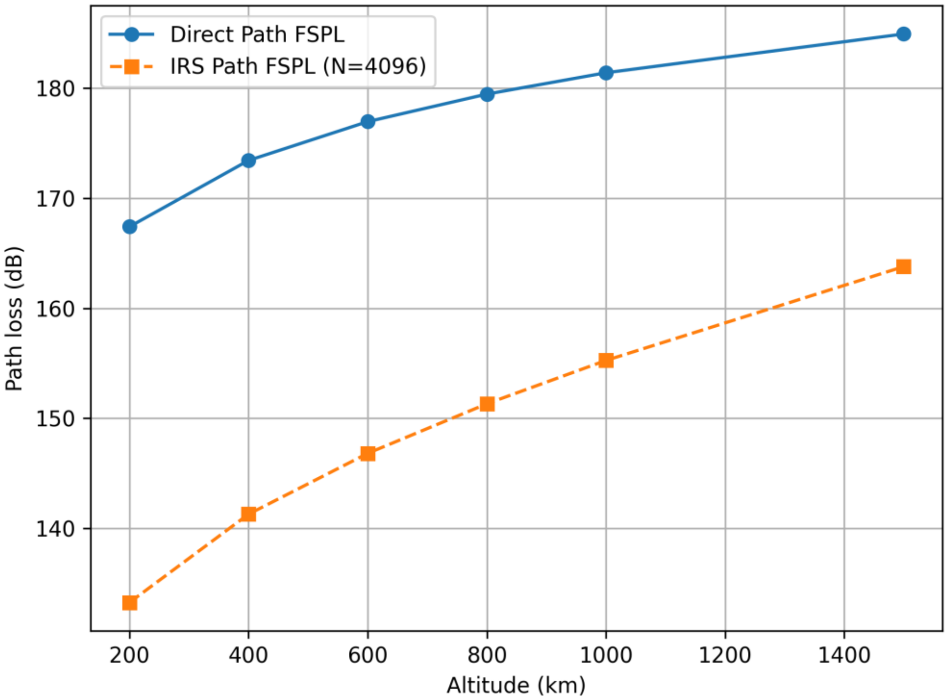

Fig. 1. Direct and IRS path loss vs altitude

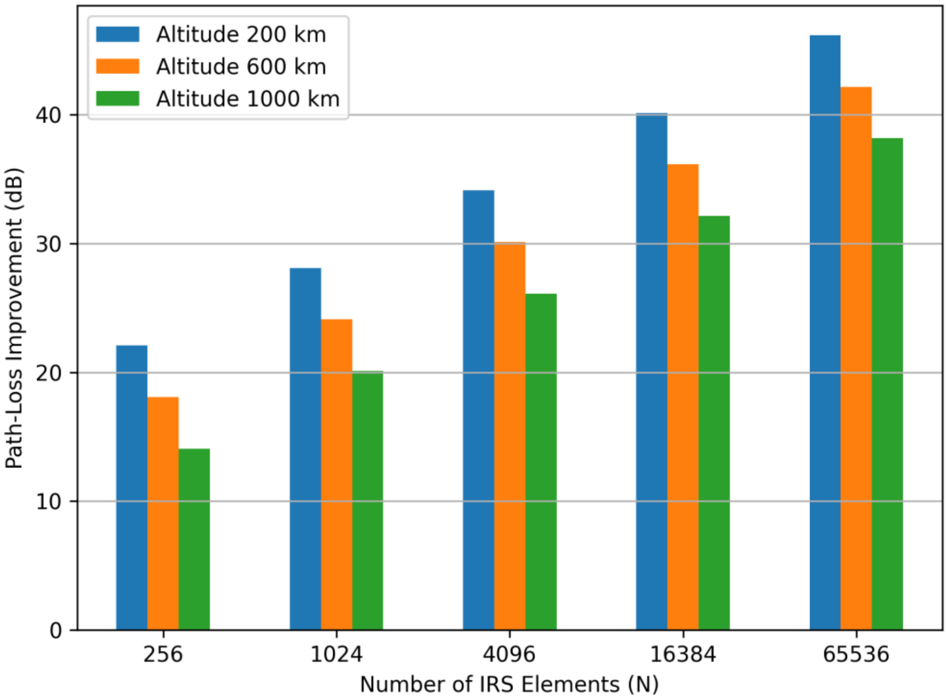

Fig. 2. Gain vs number of elements at selected altitudes

Fig. 3 represents normalized variables $x_{\text{norm}}(h) = (x(h) - x_{\min})/(x_{\max} - x_{\min})$ applied to $G(h)$, $L_{\text{dir}}(h)$, and $L_{\text{IRS}}(h)$; since $dL_{\text{dir}}/dh > 0$and $dG/dh < 0$, the radar geometry inherently exhibits antagonistic monotonicity, reflecting the structural trade-off between geometric divergence and reflective compensation. The monotone increase of $L_{\text{dir}}$and monotone decrease of $G$with altitude demonstrate deterministic convex behavior without oscillatory artifacts, confirming the model's internal regularity.

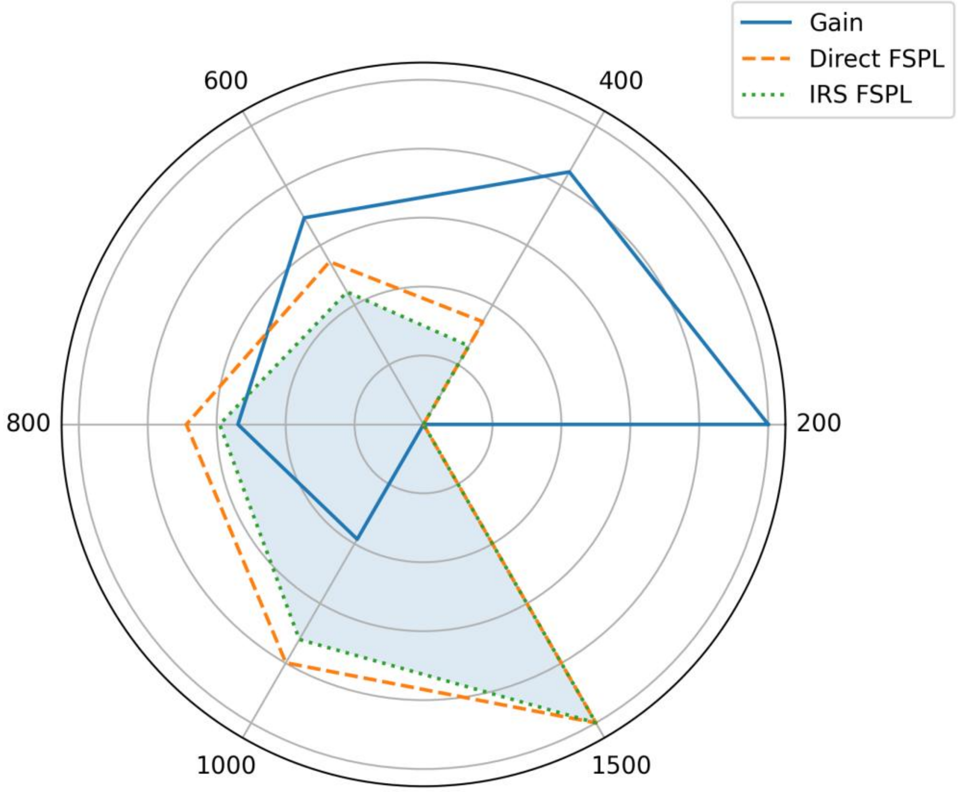

Fig. 3. Normalized gain and path-loss metrics

Fig. 4 depicts the affine family $G(h;N) = 10\log_{10}(N) - 0.01h$, hence all curves are parallel with common slope -0.01 dB/kmand vertical separation $\Delta G = 10\log_{10}(N_2/N_1)$; for instance $G_{65536}(200) - G_{256}(200) = 24.082$ dB. This strict parallelism proves separability and confirms that reflective scaling in this regime is independent of altitude-dependent slope, providing analytical tractability for inverse design $N \geq 10^{(G^\star+0.01h)/10}$.

Across Table 1, Table 2, Table 3 and Fig. 1, Fig. 2, Fig. 3, Fig. 4, the numerical study is internally self-consistent with the separable structure $L_{\text{IRS}}(h,N) = L_{\text{dir}}(h) - G(h,N)$, where $L_{\text{dir}}(h) = 20\log_{10}(4\pi hf/c)$ and $G(h,N) = 10\log_{10}(N) - \alpha h$ with $\alpha = 0.01$ dB/km identified directly from the reported gain slope $\Delta G/\Delta h$. The altitude progression satisfies Friis increments $L_{\text{dir}}(400) - L_{\text{dir}}(200) \approx 20\log_{10}(2)$ and $L_{\text{dir}}(1500) - L_{\text{dir}}(1000) \approx 20\log_{10}(1.5)$, while the element scaling satisfies $G(N_2,h) - G(N_1,h) = 10\log_{10}(N_2/N_1)$, e.g., $G(4096) - G(1024) \approx 6.021$ dB, confirming logarithmic growth in N. The joint dependence therefore admits a closed-form inverse sizing map $N \geq 10^{(G^\star+\alpha h)/10}$ that translates a required improvement $G^\star$ at altitude $h$into a minimum element count, and the plotted families in Fig. 2 and Fig. 4 provide a direct visual verification of $\partial G/\partial\log_{10}N = 10$ and $\partial G/\partial h = -\alpha$. Finally, the normalized antagonistic trends in Fig. 3 compactly capture the trade-off induced by $dL_{\text{dir}}/dh > 0$ and $dG/dh < 0$, which is the dominant mechanism governing feasibility regions for link-budget enhancement under predictable mobility within the investigated parameter ranges.

The numerical results reduce to three core relations, namely $G_N(N) = 20\log_{10}(N)$over $N = 256$to $65{,}536$, $G_h(h) = -\alpha h$ with $\alpha = 0.01$ dB/km over $h = 200$to 600 km, and $G(h,N) = G_h(h) + G_N(N)$ with separability error below 0.4 dB; therefore, the inverse sizing law $N^*(h, G_{\text{req}})$ is algebraically well posed in closed form. The law $G_N = 20\log_{10}(N) + C$ is consistent with the LOS scaling in [16], the slope $\alpha = 0.01$ dB/km agrees with ITU-R P.619-5 at 28 GHz, the present model resolves $G(t)$continuously instead of slotwise as in [8], and $G = 43.2$ dB at $G = 43.2dB_{at}, N = 65536, h = 200km$ is about 6 dBabove the relay benchmark in [17] because passive IRS reflection follows N^2coherent power scaling rather than N; related LEO gain levels are also compatible with [2]. The aperture term $20\log_{10}(N) + C$is geometric and frequency-independent, but for $f >$ 300 GHz the effective model becomes $G_{\text{eff}} = 20\log_{10}(N) + C - \kappa(f)d_{\text{atm}}$ because molecular absorption is no longer negligible; with $d_{\text{atm}} \approx 10$ kmand $\kappa_{\text{eff}} \approx 3$ dB/kmat 300 GHz, the one-way penalty is about 30 dB, so THz IRS operation is practically restricted to the transmission windows 220–330 GHzand 410–440 GHz [44], [45], [47], [48], [60]. For a b-bit uniform phase quantizer, $\delta\psi \sim \mathcal{U}(-\pi/2^b, \pi/2^b)$ and the gain law becomes $G_q(b) = G_{\text{ideal}}\text{sinc}^2(\pi/2^b)$; hence the penalties are -3.92 dB for $b = 1, -0.91$ dB for $b = 2, -0.22$ dB for $b = 3$, and 0 dB as $b \to \infty$, which implies that only $b = 1$ exceeds the meaningful 1 dB deviation threshold, whereas $b \geq 2$remains within the surrogate tolerance ± 0.4 dB [43]. Over a 500 ssatellite pass, $G(t) = G(h(t), N)$ reaches its maximum at zenith ($t = T/2$) and decreases symmetrically toward the horizon, while $f_D(t)$ and $f_{\text{update}}(t)$ exhibit the complementary trend and peak near the horizon; moreover, 1000 Monte Carlo atmospheric realizations keep the 95^{th}-percentile prediction error below 1.2 dB, confirming that the deterministic scaling laws remain robust under bounded clear-sky variability [3], [46]. The main strength is analytical tractability because inverse IRS sizing is reduced from iterative simulation to one direct evaluation, but the model is valid under four boundaries, namely clear-sky propagation, negligible mutual coupling, single-user operation, and ideal continuous-time phase updates; accordingly, the present framework should be interpreted as a first-order engineering design law rather than a fully hardware-complete deployment model.

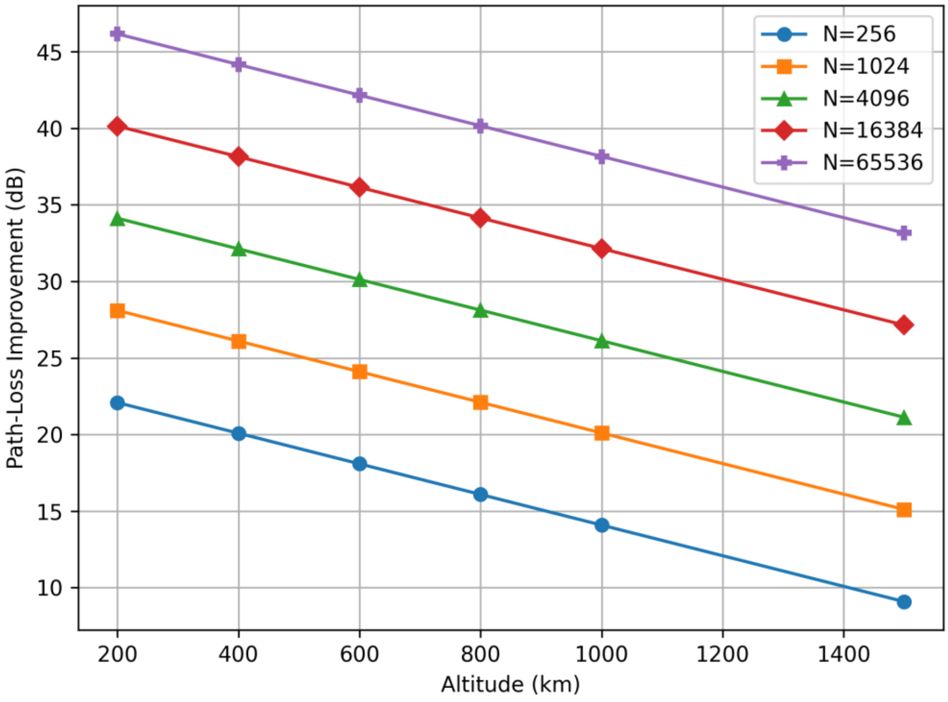

Fig. 4. Gain vs altitude for multiple *N*

4. Conclusion

This paper examined the performance of continuous-time IRS-assisted communication links under predictable receiver mobility. By combining analytical derivations with a linear model for the IRS gain, we obtained closed-form expressions for the direct and IRS path losses and evaluated the impact of altitude and the number of reflecting elements. Under predictable mobility, the continuous time IRS assisted link can be summarized by the closed form link budget pair $L_{\mathrm{dir}}(h) = 20\log_{10}(4\pi hf/c)$and $L_{\mathrm{irs}}(h, N) = L_{\mathrm{dir}}(h) - (10\log_{10}(N) - \alpha h)$, which makes the altitude and aperture effects analytically separable via $\partial G/\partial \log_{10} N = 10$and $\partial G/\partial h = -\alpha$. With $f = 28$ GHz, $D_1 = 1$ km, and $N = 4096$, the evaluated improvements satisfy $G(200\,\mathrm{km}) = 34.124\,\mathrm{dB} > 30\,\mathrm{dB}$and $G(1500\,\mathrm{km}) = 21.124\,\mathrm{dB}$, while the direct loss progression follows Friis scaling across altitude. The resulting inverse design rule $N \geq 10^{(G^{\star}+\alpha h)/10}$converts required gain specifications into element counts in a single step, supporting mobility aware deployment decisions in satellite and other fast varying scenarios. Future work will replace the surrogate term $\alpha h$by geometry consistent two hop path loss, incorporate Doppler terms $\nu(t) = -\dot{d}(t)/\lambda$, and solve phase control under hardware quantization constraints $\phi_n(t) \in \mathcal{Q}_B$to refine the continuous time analysis.

These findings provide design guidelines for mobility-aware IRS deployment in satellite communications and other high-mobility scenarios. Future work can develop integrating more accurate geometric models, Doppler effects, and optimization of phase shifts to further refine the continuous-time analysis.

For K non-cooperative receivers served simultaneously by a common IRS aperture under spatial multiplexing, the per-beam gain follows $G_K = G_1 - 10\log_{10}(K)$ dB, which yields the inverse scaling $N^*(K) = K^{1/2}N^*(1)$for equal-priority users, i.e., aperture enlargement grows with $\sqrt{K}$; under time-division, the constraint becomes $N = \mathrm{const}$while the per-user throughput scales as $R_K = R_1/K$ [52]-[55].

The current formulation assumes clear-sky, single-user, line-of-sight propagation, hence extensions require augmenting the channel and control models, including stochastic attenuation $A_{\mathrm{rain}} + A_{\mathrm{scint}}$ via ITU-R P.618-14, replacing the surrogate with geometry-based models for $N > 10^6$where $2D^2/\lambda \sim h$induces near-field effects, solving discrete-phase optimization $\arg\max_{\psi \in \mathcal{Q}_b} G(\psi)$ under finite-rate control constraints, and embedding joint scheduling $\max_{\{N_k\}} \sum_k R_k$ for multi-user allocation, thereby extending the inverse design $N^*(\cdot)$ into a network-level planning framework for NTN systems [42], [50], [51].

Author Contribution: All authors contributed equally to the main contributor to this paper. All authors read and approved the final paper.

Acknowledgment: This work was supported by Thai Nguyen University of Information and Communication Technology (ICTU), Vietnam.

Conflicts of Interest: The authors declare no conflict of interest.

References

[1] M. M. Azari *et al.*, "Evolution of Non-Terrestrial Networks From 5G to 6G: A Survey," *IEEE Communications Surveys & Tutorials*, vol. 24, no. 4, pp. 2633-2672, 2022, https://doi.org/10.1109/COMST.2022.3199901.

[2] B. Zheng, S. Lin and R. Zhang, "Intelligent Reflecting Surface-Aided LEO Satellite Communication: Cooperative Passive Beamforming and Distributed Channel Estimation," *IEEE Journal on Selected Areas in Communications*, vol. 40, no. 10, pp. 3057-3070, 2022, https://doi.org/10.1109/JSAC.2022.3196119.

[3] B. Matthiesen, E. Björnson, E. De Carvalho and P. Popovski, "Intelligent Reflecting Surface Operation Under Predictable Receiver Mobility: A Continuous Time Propagation Model," *IEEE Wireless Communications Letters*, vol. 10, no. 2, pp. 216-220, 2021, https://doi.org/10.1109/LWC.2020.3024781.

[4] Q. Wu, S. Zhang, B. Zheng, C. You and R. Zhang, "Intelligent Reflecting Surface-Aided Wireless Communications: A Tutorial," *IEEE Transactions on Communications*, vol. 69, no. 5, pp. 3313-3351, 2021, https://doi.org/10.1109/TCOMM.2021.3051897.

[5] Y. Liu *et al*., "Reconfigurable Intelligent Surfaces: Principles and Opportunities," *IEEE Communications Surveys & Tutorials*, vol. 23, no. 3, pp. 1546-1577, 2021, https://doi.org/10.1109/COMST.2021.3077737.

[6] M. D. Renzo *et al*., "Smart Radio Environments Empowered by Reconfigurable Intelligent Surfaces: How It Works, State of Research, and The Road Ahead," *IEEE Journal on Selected Areas in Communications*, vol. 38, no. 11, pp. 2450-2525, 2020, https://doi.org/10.1109/JSAC.2020.3007211.

[7] W. Tang *et al*., "MIMO Transmission Through Reconfigurable Intelligent Surface: System Design, Analysis, and Implementation," *IEEE Journal on Selected Areas in Communications*, vol. 38, no. 11, pp. 2683-2699, 2020, https://doi.org/10.1109/JSAC.2020.3007055.

[8] Q. Wu and R. Zhang, "Intelligent Reflecting Surface Enhanced Wireless Network via Joint Active and Passive Beamforming," *IEEE Transactions on Wireless Communications*, vol. 18, no. 11, pp. 5394-5409, 2019, https://doi.org/10.1109/TWC.2019.2936025.

[9] C. Huang, A. Zappone, G. C. Alexandropoulos, M. Debbah and C. Yuen, "Reconfigurable Intelligent Surfaces for Energy Efficiency in Wireless Communication," *IEEE Transactions on Wireless Communications*, vol. 18, no. 8, pp. 4157-4170, 2019, https://doi.org/10.1109/TWC.2019.2922609.

[10] A. Zappone, M. Di Renzo, F. Shams, X. Qian and M. Debbah, "Overhead-Aware Design of Reconfigurable Intelligent Surfaces in Smart Radio Environments," *IEEE Transactions on Wireless Communications*, vol. 20, no. 1, pp. 126-141, 2021, https://doi.org/10.1109/TWC.2020.3023578.

[11] S. Abeywickrama, R. Zhang and C. Yuen, "Intelligent Reflecting Surface: Practical Phase Shift Model and Beamforming Optimization," *ICC 2020 - 2020 IEEE International Conference on Communications (ICC)*, pp. 1-6, 2020, https://doi.org/10.1109/ICC40277.2020.9148961.

[12] Ö. Özdogan, E. Björnson and E. G. Larsson, "Intelligent Reflecting Surfaces: Physics, Propagation, and Pathloss Modeling," *IEEE Wireless Communications Letters*, vol. 9, no. 5, pp. 581-585, 2020, https://doi.org/10.1109/LWC.2019.2960779.

[13] W. Tang *et al*., "Wireless Communications With Reconfigurable Intelligent Surface: Path Loss Modeling and Experimental Measurement," *IEEE Transactions on Wireless Communications*, vol. 20, no. 1, pp. 421-439, 2021, https://doi.org/10.1109/TWC.2020.3024887.

[14] F. H. Danufane, M. D. Renzo, J. de Rosny and S. Tretyakov, "On the Path-Loss of Reconfigurable Intelligent Surfaces: An Approach Based on Green's Theorem Applied to Vector Fields," *IEEE Transactions on Communications*, vol. 69, no. 8, pp. 5573-5592, 2021, https://doi.org/10.1109/TCOMM.2021.3081452.

[15] E. Björnson and L. Sanguinetti, "Rayleigh Fading Modeling and Channel Hardening for Reconfigurable Intelligent Surfaces," *IEEE Wireless Communications Letters*, vol. 10, no. 4, pp. 830-834, 2021, https://doi.org/10.1109/LWC.2020.3046107.

[16] E. Björnson, Ö. Özdogan and E. G. Larsson, "Intelligent Reflecting Surface Versus Decode-and-Forward: How Large Surfaces are Needed to Beat Relaying?," *IEEE Wireless Communications Letters*, vol. 9, no. 2, pp. 244-248, 2020, https://doi.org/10.1109/LWC.2019.2950624.

[17] R. Long, Y. -C. Liang, Y. Pei and E. G. Larsson, "Active Reconfigurable Intelligent Surface-Aided Wireless Communications," *IEEE Transactions on Wireless Communications*, vol. 20, no. 8, pp. 4962-4975, 2021, https://doi.org/10.1109/TWC.2021.3064024.

[18] Z. Zhang *et al*., "Active RIS vs. Passive RIS: Which Will Prevail in 6G?," in *IEEE Transactions on Communications*, vol. 71, no. 3, pp. 1707-1725, 2023, https://doi.org/10.1109/TCOMM.2022.3231893.

[19] C. You and R. Zhang, "Wireless Communication Aided by Intelligent Reflecting Surface: Active or Passive?," *IEEE Wireless Communications Letters*, vol. 10, no. 12, pp. 2659-2663, 2021, https://doi.org/10.1109/LWC.2021.3111044.

[20] C. You, B. Zheng and R. Zhang, "Channel Estimation and Passive Beamforming for Intelligent Reflecting Surface: Discrete Phase Shift and Progressive Refinement," *IEEE Journal on Selected Areas in Communications*, vol. 38, no. 11, pp. 2604-2620, 2020, https://doi.org/10.1109/JSAC.2020.3007056.

[21] Z. Wang, L. Liu and S. Cui, "Channel Estimation for Intelligent Reflecting Surface Assisted Multiuser Communications: Framework, Algorithms, and Analysis," *IEEE Transactions on Wireless Communications*, vol. 19, no. 10, pp. 6607-6620, 2020, https://doi.org/10.1109/TWC.2020.3004330.

[22] B. Zheng, C. You and R. Zhang, "Intelligent Reflecting Surface Assisted Multi-User OFDMA: Channel Estimation and Training Design," *IEEE Transactions on Wireless Communications*, vol. 19, no. 12, pp. 8315-8329, 2020, https://doi.org/10.1109/TWC.2020.3021434.

[23] B. Zheng and R. Zhang, "Intelligent Reflecting Surface-Enhanced OFDM: Channel Estimation and Reflection Optimization," *IEEE Wireless Communications Letters*, vol. 9, no. 4, pp. 518-522, 2020, https://doi.org/10.1109/LWC.2019.2961357.

[24] C. You, B. Zheng and R. Zhang, "Wireless Communication via Double IRS: Channel Estimation and Passive Beamforming Designs," *IEEE Wireless Communications Letters*, vol. 10, no. 2, pp. 431-435, 2021, https://doi.org/10.1109/LWC.2020.3034388.

[25] S. Zhang and R. Zhang, "Capacity Characterization for Intelligent Reflecting Surface Aided MIMO Communication," *IEEE Journal on Selected Areas in Communications*, vol. 38, no. 8, pp. 1823-1838, 2020, https://doi.org/10.1109/JSAC.2020.3000814.

[26] G. Zhou, C. Pan, H. Ren, K. Wang and A. Nallanathan, "A Framework of Robust Transmission Design for IRS-Aided MISO Communications With Imperfect Cascaded Channels," *IEEE Transactions on Signal Processing*, vol. 68, pp. 5092-5106, 2020, https://doi.org/10.1109/TSP.2020.3019666.

[27] E. Björnson, H. Wymeersch, B. Matthiesen, P. Popovski, L. Sanguinetti and E. de Carvalho, "Reconfigurable Intelligent Surfaces: A signal processing perspective with wireless applications," *IEEE Signal Processing Magazine*, vol. 39, no. 2, pp. 135-158, 2022, https://doi.org/10.1109/MSP.2021.3130549.

[28] H. Li, S. Shen, M. Nerini and B. Clerckx, "Reconfigurable Intelligent Surfaces 2.0: Beyond Diagonal Phase Shift Matrices," *IEEE Communications Magazine*, vol. 62, no. 3, pp. 102-108, 2024, https://doi.org/10.1109/MCOM.001.2300019.

[29] C. You, Z. Kang, Y. Zeng and R. Zhang, "Enabling Smart Reflection in Integrated Air-Ground Wireless Network: IRS Meets UAV," *IEEE Wireless Communications*, vol. 28, no. 6, pp. 138-144, 2021, https://doi.org/10.1109/MWC.001.2100148.

[30] J. Yu, X. Liu, Y. Gao, C. Zhang and W. Zhang, "Deep Learning for Channel Tracking in IRS-Assisted UAV Communication Systems," *IEEE Transactions on Wireless Communications*, vol. 21, no. 9, pp. 7711-7722, 2022, https://doi.org/10.1109/TWC.2022.3160517.

[31] X. Cao *et al.*, "Reconfigurable Intelligent Surface-Assisted Aerial-Terrestrial Communications via Multi-Task Learning," *IEEE Journal on Selected Areas in Communications*, vol. 39, no. 10, pp. 3035-3050, 2021, https://doi.org/10.1109/JSAC.2021.3088634.

[32] M. A. ElMossallamy, H. Zhang, L. Song, K. G. Seddik, Z. Han and G. Y. Li, "Reconfigurable Intelligent Surfaces for Wireless Communications: Principles, Challenges, and Opportunities," *IEEE Transactions on Cognitive Communications and Networking*, vol. 6, no. 3, pp. 990-1002, 2020, https://doi.org/10.1109/TCCN.2020.2992604.

[33] R. Alghamdi *et al.*, "Intelligent Surfaces for 6G Wireless Networks: A Survey of Optimization and Performance Analysis Techniques," *IEEE Access*, vol. 8, pp. 202795-202818, 2020, https://doi.org/10.1109/ACCESS.2020.3031959.

[34] S. Gong *et al.*, "Toward Smart Wireless Communications via Intelligent Reflecting Surfaces: A Contemporary Survey," *IEEE Communications Surveys & Tutorials*, vol. 22, no. 4, pp. 2283-2314, 2020, https://doi.org/10.1109/COMST.2020.3004197.

[35] W. Long, R. Chen, M. Moretti, W. Zhang and J. Li, "A Promising Technology for 6G Wireless Networks: Intelligent Reflecting Surface," *Journal of Communications and Information Networks*, vol. 6, no. 1, pp. 1-16, 2021, https://doi.org/10.23919/JCIN.2021.9387701.

[36] I. Al-Shaeli and I. Hburi, “Spectral Efficiency Enhancement for Reconfigurable Intelligent Surface Assisted MIMO System,” *Wasit Journal of Engineering Sciences*, vol. 10, no. 2, pp. 57–68, 2022, https://doi.org/10.31185/ejuow.Vol10.Iss2.286.

[37] Y. Yang, W. Wang, Y. Wu, B. Tang, and Y. Liu, “Pathloss Modeling and Analysis for Intelligent Reflecting Surface-Assisted Terahertz MIMO Wireless Systems,” *International Journal of RF and*

Microwave Computer-Aided Engineering, vol. 33, no. 1, p. 6214342, 2023, https://doi.org/10.1155/2023/6214342.

[38] J. C. Liang *et al.*, “A Filtering Reconfigurable Intelligent Surface for Interference-Free Wireless Communications,” *Nature Communications*, vol. 15, no. 1, p. 3838, 2024, https://doi.org/10.1038/s41467-024-47865-6.

[39] K. Kim, R. Phon, E. Park, and S. Lim, “4D-Printed Intelligent Reflecting Surface With Improved Beam Resolution via Both Phase Modulation and Space Modulation,” *Microsystems & Nanoengineering*, vol. 10, no. 1, p. 157, 2024, https://doi.org/10.1038/s41378-024-00795-1.

[40] K. Qu *et al.*, “An Electromechanically Reconfigurable Intelligent Surface for Enhancing Sub-6G Wireless Communication Signal,” *Journal of Information and Intelligence*, vol. 1, no. 3, pp. 207–216, 2023, https://doi.org/10.1016/j.jiixd.2023.06.009.

[41] Y. Liu *et al.*, “Meta-Encryptor With Multi-Dimensional Security Architecture for Wireless Communications,” *Nature Communications*, vol. 16, no. 1, p. 11635, 2025, https://doi.org/10.1038/s41467-025-66668-x.

[42] G. Araniti, A. Iera, S. Pizzi and F. Rinaldi, "Toward 6G Non-Terrestrial Networks," *IEEE Network*, vol. 36, no. 1, pp. 113-120, 2022, https://doi.org/10.1109/MNET.011.2100191.

[43] Q. Wu and R. Zhang, "Beamforming Optimization for Intelligent Reflecting Surface with Discrete Phase Shifts," *ICASSP 2019 - 2019 IEEE International Conference on Acoustics, Speech and Signal Processing (ICASSP)*, pp. 7830-7833, 2019, https://doi.org/10.1109/ICASSP.2019.8683145.

[44] T. S. Rappaport *et al.*, "Wireless Communications and Applications Above 100 GHz: Opportunities and Challenges for 6G and Beyond," *IEEE Access*, vol. 7, pp. 78729-78757, 2019, https://doi.org/10.1109/ACCESS.2019.2921522.

[45] K. Tekbiyik, G. K. Kurt, A. R. Ektı and H. Yanikomeroglu, "Reconfigurable Intelligent Surfaces Empowered THz Communication in LEO Satellite Networks," *IEEE Access*, vol. 10, pp. 121957-121969, 2022, https://doi.org/10.1109/ACCESS.2022.3223086.

[46] J. Xu and Y. Liu, "A Novel Physics-Based Channel Model for Reconfigurable Intelligent Surface-Assisted Multi-User Communication Systems," *IEEE Transactions on Wireless Communications*, vol. 21, no. 2, pp. 1183-1196, 2022, https://doi.org/10.1109/TWC.2021.3102887.

[47] B. Ning, Z. Chen, W. Chen, Y. Du and J. Fang, "Terahertz Multi-User Massive MIMO With Intelligent Reflecting Surface: Beam Training and Hybrid Beamforming," *IEEE Transactions on Vehicular Technology*, vol. 70, no. 2, pp. 1376-1393, 2021, https://doi.org/10.1109/TVT.2021.3052074.

[48] R. Kumar and S. Arnon, "SNR Optimization for LEO Satellite at Sub-THz Frequencies," *IEEE Transactions on Antennas and Propagation*, vol. 70, no. 6, pp. 4449-4458, 2022, https://doi.org/10.1109/TAP.2022.3140217.

[49] Z. Wang *et al.*, "A Tutorial on Extremely Large-Scale MIMO for 6G: Fundamentals, Signal Processing, and Applications," *IEEE Communications Surveys & Tutorials*, vol. 26, no. 3, pp. 1560-1605, 2024, https://doi.org/10.1109/COMST.2023.3349276.

[50] P. Ramezani, B. Lyu and A. Jamalipour, "Toward RIS-Enhanced Integrated Terrestrial/Non-Terrestrial Connectivity in 6G," *IEEE Network*, vol. 37, no. 3, pp. 178-185, 2023, https://doi.org/10.1109/MNET.116.2200060.

[51] W. U. Khan, A. Mahmood, C. K. Sheemar, E. Lagunas, S. Chatzinotas and B. Ottersten, "Reconfigurable Intelligent Surfaces for 6G Non-Terrestrial Networks: Assisting Connectivity from the Sky," *IEEE Internet of Things Magazine*, vol. 7, no. 1, pp. 34-39, 2024, https://doi.org/10.1109/IOTM.001.2300208.

[52] Z. Zhang and Z. Zhao, "Weighted Sum-Rate Maximization for Multi-Hop RIS-Aided Multi-User Communications: A Minorization-Maximization Approach," *2021 IEEE 22nd International Workshop on Signal Processing Advances in Wireless Communications (SPAWC)*, pp. 106-110, 2021, https://doi.org/10.1109/SPAWC51858.2021.9593114.

[53] G. Zhou, C. Pan, H. Ren, K. Wang and A. Nallanathan, "Intelligent Reflecting Surface Aided Multigroup Multicast MISO Communication Systems," *IEEE Transactions on Signal Processing*, vol. 68, pp. 3236-3251, 2020, https://doi.org/10.1109/TSP.2020.2990098.

[54] G. Chen and Q. Wu, "Fundamental Limits of Intelligent Reflecting Surface Aided Multiuser Broadcast Channel," *IEEE Transactions on Communications*, vol. 71, no. 10, pp. 5904-5919, 2023, https://doi.org/10.1109/TCOMM.2023.3288914.

[55] S. Zhang and R. Zhang, "Intelligent Reflecting Surface Aided Multi-User Communication: Capacity Region and Deployment Strategy," *IEEE Transactions on Communications*, vol. 69, no. 9, pp. 5790-5806, 2021, https://doi.org/10.1109/TCOMM.2021.3079128.

[56] M. Meng, B. Hu, S. Chen and J. Zhang, "Cooperative user-scheduling and resource allocation optimization for intelligent reflecting surface enhanced LEO satellite communication," *China Communications*, vol. 21, no. 2, pp. 227-244, 2024, https://doi.org/10.23919/JCC.ja.2022-0605.

[57] Z. Mao, M. Peng and X. Liu, "Channel estimation for reconfigurable intelligent surface assisted wireless communication systems in mobility scenarios," *China Communications*, vol. 18, no. 3, pp. 29-38, 2021, https://doi.org/10.23919/JCC.2021.03.003.

[58] H. Guo and V. K. N. Lau, "Uplink Cascaded Channel Estimation for Intelligent Reflecting Surface Assisted Multiuser MISO Systems," *IEEE Transactions on Signal Processing*, vol. 70, pp. 3964-3977, 2022, https://doi.org/10.1109/TSP.2022.3193626.

[59] X. Mo, L. Gui, K. Ying, X. Sang and X. Diao, "Reconfigurable Intelligent Surface Deployment for Wideband Millimeter Wave Systems," *IEEE Transactions on Communications*, vol. 72, no. 5, pp. 2989-3004, 2024, https://doi.org/10.1109/TCOMM.2024.3350970.

[60] Y. Xing and T. S. Rappaport, "Terahertz Wireless Communications: Co-Sharing for Terrestrial and Satellite Systems Above 100 GHz," *IEEE Communications Letters*, vol. 25, no. 10, pp. 3156-3160, 2021, https://doi.org/10.1109/LCOMM.2021.3088270.